# Nanoparticles size-dependently initiate self-limiting NETosis-driven inflammation

Luis E. Muñoz[a,1], Rostyslav Bilyy[a,b,1], Mona H. C. Biermann[a,1], Deborah Kienhöfer[a], Christian Maueröder[a], Jonas Hahn[a], Jan M. Brauner[a], Daniela Weidner[a], Jin Chen[a,c], Marina Scharin-Mehlmann[d], Christina Janko[e], Ralf P. Friedrich[e], Dirk Mielenz[f], Tetiana Dumych[b], Maxim D. Lootsik[b], Christine Schauer[a], Georg Schett[a], Markus Hoffmann[a], Yi Zhao[a,c,2,3], and Martin Herrmann[a,2,3]

[a]Department of Internal Medicine 3–Rheumatology and Immunology, Universitätsklinikum Erlangen, Friedrich-Alexander-Universität Erlangen-Nürnberg, 91054 Erlangen, Germany; [b]Danylo Halytsky Lviv National Medical University, 79010 Lviv, Ukraine; [c]Department of Rheumatology and Immunology, West China Hospital, Sichuan University, 610041 Chengdu, Sichuan Province, China; [d]Electron Devices, Friedrich-Alexander-Universität Erlangen-Nürnberg, Erlangen 91058, Germany; [e]Section for Experimental Oncology and Nanomedicine, Department of Otorhinolaryngology, Head, and Neck Surgery, University Hospital Erlangen, 91054 Erlangen, Germany; and [f]Division of Molecular Immunology, Department of Internal Medicine 3, Nikolaus Fiebiger Center, Friedrich-Alexander-Universität Erlangen-Nürnberg, 91054 Erlangen, Germany

Edited by Mauro Ferrari, The Methodist Hospital Research Institute, Houston, TX, and accepted by Editorial Board Member Carl F. Nathan August 3, 2016 (received for review February 11, 2016)

**The critical size for strong interaction of hydrophobic particles with phospholipid bilayers has been predicted to be 10 nm. Because of the wide spreading of nonpolar nanoparticles (NPs) in the environment, we aimed to reveal the ability of living organisms to entrap NPs via formation of neutrophil extracellular traps (NETs). Upon interaction with various cell types and tissues, 10- to 40-nm-sized NPs induce fast (<20 min) damage of plasma membranes and instability of the lysosomal compartment, leading to the immediate formation of NETs. In contrast, particles sized 100–1,000 nm behaved rather inertly. Resulting NET formation (NETosis) was accompanied by an inflammatory reaction intrinsically endowed with its own resolution, demonstrated in lungs and air pouches of mice. Persistence of small NPs in joints caused unremitting arthritis and bone remodeling. Small NPs coinjected with antigen exerted adjuvant-like activity. This report demonstrates a cellular mechanism that explains how small NPs activate the NETosis pathway and drive their entrapping and resolution of the initial inflammatory response.**

nanoparticles | size | neutrophils | NETosis | inflammation

Recent advances of nanotechnology have resulted in an unprecedented exposure of the human organism to nanomaterials. Among these nanomaterials are highly hydrophobic, chemically inert nanoparticles (NPs). The strategy of the human body to cope with hydrophobic substances is based on their oxidation, conjugation with more soluble hydrophilic adducts, and removal via excretion. This process is exemplified by the oxidative removal of bilirubin by the liver via the bile fluid. However, if inert hydrophobic material withstands oxidation, it escapes the regular clearance mechanisms.

Here, we investigated the effect of two common sources of NPs: carbon and polystyrene nanopowders. We used chemically identical material of various sizes to study their interactions with the innate immune system. Both NP types are abundant in the environment. Carbon NPs (nanodiamonds) accompany naturally occurring meteors and are man-made materials generated by abrasive techniques, laser printing, smoke, and smog. Polystyrene NPs are ubiquitously found in manufacturing. The knowledge of recognition and clearance pathways for these NP types is rather limited, especially for those materials that have passed the body's surface barriers and entered tissues. However, the following are well known. (*i*) Nanodiamond films support adhesion and differentiation of osteogenic cells, being candidates for surface modification of implants to improve their integration into the bone (1). The recent development of fullerenes and carbon nanotubes holds high technical potential and may considerably increase the contact of nanomaterial with the biosphere (2). (*ii*) Recent in silico data (3) have demonstrated that the sizes of NPs greatly influence their interaction with biological membranes possessing lipid asymmetry. For strong and (ultra)-weak adhesion, the critical particle sizes were reported to be 10 nm and 1 μm, respectively (3). The increased hydrophobicity of gold NPs smaller than 10 nm has been correlated linearly with an enhanced expression of proinflammatory cytokines in splenocytes isolated from mice (4).

Therefore, it is not surprising that mechanisms have been developed to cope with the exposure to NPs without triggering inflammatory responses. Indeed, phagocytosis, excretion, catabolism, isolation, and immobilization are strategies of the body to handle or ideally clear NPs. Although this process is usually silent, they can also trigger inflammatory responses. For instance, in patients with asthma, inhaled carbon nanotubes reportedly aggravate lung disease (5). Several cells orchestrate the response to particulate agents. Epithelial cells constitute physical barriers, mononuclear phagocytes engulf and clear NPs, and granulocytes immobilize and sequester NPs, occasionally leading to granuloma formation (6).

## Significance

**The current widespread exposure of humans to natural as well as man-made nanomaterials due to the deployment of nanoparticles (NPs) as food additives, as vaccine- or drug-delivery vehicles, and in diagnostic procedures encourages the evaluation of their interaction with the innate immune system. Understanding how organisms cope with hydrophobic and chemically inert particulate matter, which is excluded from metabolic processing, is of major importance for interpreting the responses associated with the use of NPs in the biosphere. The containment of NPs within neutrophil-derived aggregates locally orchestrates the resolution of inflammation. Overriding this mechanism bears the risk of inducing chronic inflammation and causing tissue damage.**

Author contributions: L.E.M., R.B., G.S., Y.Z., and M. Herrmann designed research; L.E.M., R.B., M.H.C.B., D.K., C.M., J.H., J.M.B., D.W., J.C., C.J., R.P.F., T.D., M.D.L., C.S., G.S., Y.Z., and M. Herrmann performed research; D.K., J.H., D.W., M.S.-M., C.J., R.P.F., D.M., T.D., M.D.L., and M. Hoffmann contributed new reagents/analytic tools; L.E.M., R.B., M.H.C.B., D.K., C.M., J.H., J.C., M.S.-M., C.J., R.P.F., D.M., T.D., M.D.L., C.S., M. Hoffmann, Y.Z., and M. Herrmann analyzed data; and L.E.M., R.B., M.H.C.B., C.M., G.S., M. Hoffmann, Y.Z., and M. Herrmann wrote the paper.

The authors declare no conflict of interest.

This article is a PNAS Direct Submission. M.F. is a Guest Editor invited by the Editorial Board.

[1]L.E.M., R.B., and M.H.C.B. contributed equally to this work.

[2]Y.Z. and M. Herrmann contributed equally to this work.

[3]To whom correspondence may be addressed. Email: zhao.y1977@163.com or martin.herrmann@uk-erlangen.de.

This article contains supporting information online at www.pnas.org/lookup/suppl/doi:10.1073/pnas.1602230113/-/DCSupplemental.

**Table 1. Physical-chemical properties of NPs**

| Particle | Abbreviation | Measured size, nm: TEM | Measured size, nm: DLS | Chemistry | ζ-Potential, mV | Surface |
|---|---|---|---|---|---|---|
| Polystyrene, 40 nm | $b_{40}$ | | 10%: 37; 50%: 45; 90%: 54 | Polystyrene | −30.2 ± 0.7 | Nonpolar |
| Polystyrene, 100 nm | $b_{100}$ | | 10%: 87.2; 50%: 102.3; 90%: 120.4 | Polystyrene | −33.7 ± 1.4 | Nonpolar |
| Polystyrene, 200 nm | $b_{200}$ | | 10%: 187.5; 50%: 222.3; 90%: 263.8 | Polystyrene | −41.8 ± 0.1 | Nonpolar |
| Polystyrene, 500 nm | $b_{500}$ | | 10%: 428.3; 50%: 499.4; 90%: 548.5 | Polystyrene | −51.9 ± 0.1 | Nonpolar |
| Polystyrene, 1,000 nm | $b_{1000}$ | | 10%: 837.6; 50%: 969.0; 90%: 1119 | Polystyrene | −61.9 ± 0.1 | Nonpolar |
| Diamond-PEG, 10 nm | $d_{10PEG}$ | 11 ± 2 | 105 ± 2* | Diamond with PEG | +32.0 ± 1.0 | Polar |
| Diamond, 10 nm | $d_{10}$ | 11 ± 2 | 618 ± 25* | Diamond | +33.9 ± 0.3 | Nonpolar |
| Diamond, 50 nm | $d_{50}$ | 80 ± 30 | 254 ± 15* | Diamond | −33.9 ± 0.5 | Nonpolar |
| Diamond, 200 nm | $d_{200}$ | 250 ± 50 | 274 ± 12 | Diamond | −38.9 ± 0.6 | Nonpolar |
| Diamond, 1,000 nm | $d_{1000}$ | 1,010 ± 300 | 970 ± 50 | Diamond | −37.7 ± 0.6 | Nonpolar |

%, percentile.
*A result of aggregation in aqueous solution.

In response to exogenous (bacteria, fungi, and fine dust) as well as endogenous (cholesterol and urate crystals) stimuli, neutrophil granulocytes form neutrophil extracellular traps (NETs) (7). The process involves a rapid externalization of chromatin (8). NET formation (NETosis) depends on reactive oxygen species (ROS) (9) and involves the receptor-interacting serine/threonine-protein kinase 3 (RIPK3) and the mixed lineage kinase domain-like (MLKL) of the necroptosis pathway (10) and various granular enzymes like myeloperoxidase (MPO) and neutrophil elastase (NE) (11). Importantly, neutrophil-driven inflammation is often self-limiting. Aggregated NETs (aggNETs), which are generated under high neutrophil densities, are prone to trap and proteolytically degrade proinflammatory mediators. Although NETs are initially proinflammatory, their aggregation promotes the resolution of inflammation (12). Based on these facts, we aimed to analyze the ability of neutrophils to inactivate and neutralize NPs via NETosis and aggNET formation. We observed plasma membrane (PM) damage as well as lysosomal instability, and demonstrated that NPs trigger NETosis in a size-dependent manner. In vivo models confirmed the immobilization and entrapment of NPs by NETs, limiting the initial inflammatory response that would otherwise cause tissue damage. Finally, we propose a cellular mechanism by which small-sized NPs induce direct cell damage and initiate a neutrophil-dependent pathway that leads to the resolution of inflammation and prevents tissue damage.

## Results and Discussion

**Characterization of the NPs.** Before biological assays, the physical properties of the polystyrene beads and the nanodiamonds were analyzed. Their physicochemical properties and abbreviations used are summarized in Table 1. Examination by dynamic light scattering (DLS) of polystyrene beads (b) in aqueous solution confirmed their denoted sizes (from $b_{40}$ = 40 nm to $b_{1,000}$ = 1,000 nm) (Fig. 1*A*). The stability of colloidal dispersions of beads (expressed as ζ-potential) increased with particle size (Fig. 1*B*). Nanodiamonds (d), especially at smaller sizes ($d_{10}$ = 10 nm), were highly prone to aggregate in aqueous solutions, resulting in exaggerated DLS values (Table 1). Additional physical information for $d_{10}$ is provided in Fig. 1*C*. To evaluate the relevance of the hydrophobicity of diamonds, PEGylated $d_{10}$ ($d_{10PEG}$) with a polar surface was also generated. Transmission electron microscopy (Fig. 1*D*) showed similar sizes for $d_{10}$ and $d_{10PEG}$. We used scanning electron

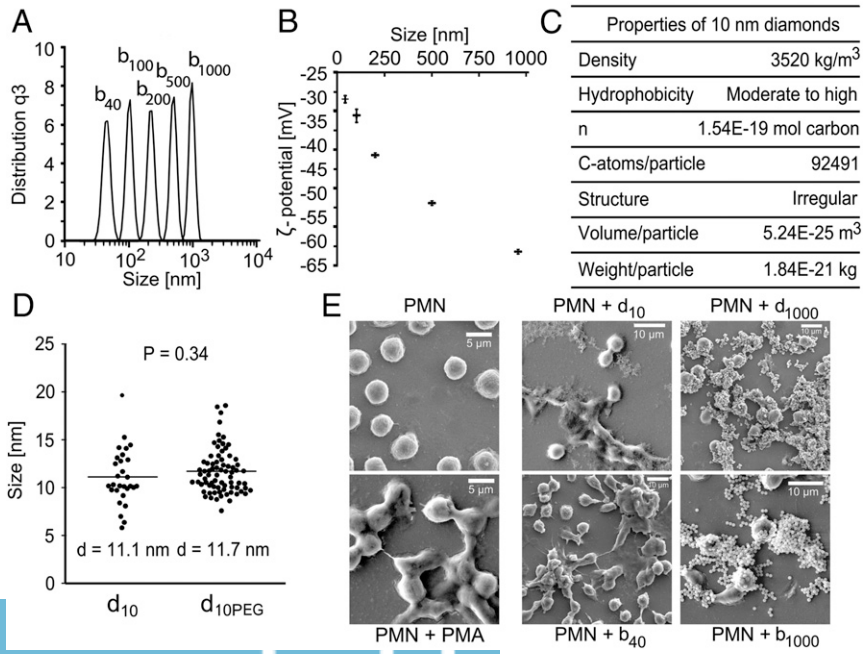


**Fig. 1.** Characteristics of the polystyrene nanobeads and nanodiamonds. (*A*) Size distribution of different polystyrene beads in water was analyzed with DLS. Depicted is the particle size distribution (q3) of a dispersion of polystyrene beads in water. (*B*) ζ-Potential of polystyrene beads in PBS by DLS. ζ-Potentials above +30 mV and below −30 mV indicate moderate to excellent stability. (*C*) Depicted are the physical data of both diamonds in general and of the 10-nm diamond NPs used in this work. (*D*) Diameter of 10-nm diamonds and PEGylated 10-nm diamonds was determined with transmission electron microscopy and subjected to morphometric analysis. Statistical analysis was performed with Welch's *t* test. (*E*) Freshly isolated polymorphonuclear (PMN) granulocytes treated with PMA. Various sizes of polystyrene beads ($b_{40}$ and $b_{1,000}$) or diamonds ($d_{10}$ and $d_{1,000}$) were analyzed by SEM. Subscripted numbers indicate particle size in nanometers.

microscopy (SEM) to investigate the effect of various types and sizes of particles on isolated human granulocytes. Phorbol 12-myristate 13-acetate (PMA) and mock-treated cells were used as established positive and negative controls, respectively, for the induction of NETs. Incubation of granulocytes with small NPs ($d_{10}$ and $b_{40}$) induced the formation of NET-like structures reminiscent of PMA-induced NETs (7) (Fig. 1*E*). In contrast, NET-like structures were not observed when granulocytes were incubated with larger NPs ($d_{1,000}$ or $b_{1,000}$), although morphologically intact granulocytes coaggregated with these particles. We conclude that both unipolar diamonds and polystyrene beads with definite characteristics size-dependently induce the formation of NET-like structures in vitro.

**Size-Dependent Induction of Membrane Damage by NPs.** There is no evidence of specific receptor-mediated uptake of NPs into neutrophils. However, due to their high hydrophobicity, NPs directly interact with lipids of cell membranes. We therefore investigated the effect of nanodiamonds of various sizes on PMs of various cell types. First, we used red blood cells (RBCs) that show neither phagocytic activity nor receptor-mediated uptake. We incubated carboxyfluorescein diacetate-labeled RBCs with diamonds of various sizes and analyzed the changes in their morphology by flow cytometry and their membrane integrity by light microscopy and by hemoglobin leakage. Nanodiamonds of all sizes led to increased granularity of RBCs (side scatter in FACS) reflecting the interaction of RBCs with the diamonds. Only small NPs ($d_{10}$) additionally enhanced forward scatter of RBCs (Fig. 2*A*), reflecting morphological changes of the RBCs. The sizes of the RBC pellets assessed on conic well plates significantly decreased after $d_{10}$ challenge compared with larger NPs (Fig. 2*B*). The release of hemoglobin from RBCs exposed to $d_{10}$ finally confirmed size-dependent damage of the PM caused by nanodiamonds (Fig. 2*C*). In accordance, the absorbance spectrum of the supernatants of RBCs incubated with $d_{10}$ shows characteristic hemoglobin peaks at 410 nm, 540 nm, and 580 nm (Fig. S1*A*). The damage caused to erythrocyte membranes by NPs was not attributable to activation of the complement system because all NPs activated the complement cascade to the same extent and regardless of their size (Fig. S1 *B* and *C*).

Next, we elucidated the interaction of nanodiamonds with epithelial (HeLa) cells possessing a contractile cytoskeleton anchored to the PM. Epithelial cells were used because they are exposed to environmental NPs at biological barriers. Again, only small NPs ($d_{10}$) (Fig. S1 *D–F*) exhibited cytotoxicity associated with vacuolization (Fig. S1*D*) as recently described for incubation with the small hydrophobic molecule vacquinol-1 (13). At the site of contact with $d_{10}$, HeLa cells formed membrane-enclosed vacuoles (Fig. S1*G*), rapidly swelled, and formed structures resembling apoptotic subcellular microvesicles (ACMVs) (Fig. 2*D* and Movie S1). Furthermore, rapid reorganization of cellular components occurred as nuclear material was extensively released into ACMV-like blebs (Movie S2). In contrast, NPs larger than 50 nm failed to establish functional associations with biological membranes (Fig. S1 *D–F*). The lipid composition of diamond-bound vacuoles, namely, the gel phase (with cholesterol) and the liquid phase (without cholesterol), was not different from the liquid composition of the PM if judged by fluorescence of the solvatochromic dye 4′-*N*,*N*-diethylamino-6-(*N*,*N*,*N*-dodecyl-methylamino-sulfopropyl)-methyl-3-hydroxyflavone (14) (Fig. S1*G*). This finding indicates that $d_{10}$ interacts with lipid components of the PM without selective preference.

Similar damage on the PM was observed with human monocyte-derived macrophages (Fig. 2*E*). As expected for such extensive membrane damage, the coincubation of $d_{10}$ with bone marrow-derived macrophages or dendritic cells did not result in cytokine production (Fig. S1*H*). Incubation with the pan-caspase inhibitor Z-VAD-FMK did not abrogate formation of such ACMV-like structures (Fig. 2*E*), suggesting that $d_{10}$ operates via direct membrane damage rather than through canonical apoptosis. Similar effects were also observed in nonadherent Jurkat cells (Fig. S2*A*). Thus, nanodiamonds induce PM damage across several different cells. The findings in epithelial cells are particularly important because these cells build up biological barriers and may be relevant for administration of nanotherapeutics. Recently, Blanco et al. (15) emphasized the importance of these barriers for exploiting the clinical potential of NP-based drug delivery (15). In this regard, NP size and geometry play a major role in their biodistribution (16–18). The challenge of certain NP-delivered drugs to pass biological barriers associated with their opsonization and sequestration by monocytes limits their site-specific bioavailability. Hence, several studies highlight the importance of innovative NP design to overcome biological barriers (19, 20). Furthermore, our results also provide experimental support for previous theoretical studies. Computational membrane modeling has allowed for establishment of the relationship between particle size, adhesive strength, and spontaneous curvature of the membrane bilayer. Two critical particle sizes were calculated and determine the strength of interaction with lipid membranes, namely, 10 nm for strong adhesion and 1,000 nm for weak adhesion (3), thus providing the mathematical background for the observed phenomena.

**Size-Dependent Induction of Lysosomal Damage in Granulocytes by NPs.** Incubation of freshly isolated granulocytes (blue intracellular nuclei) with $d_{10}$ resulted in rapid rupture of the PM and release of DNA [stained red with the membrane-impermeant DNA dye propidium iodide (PI)]. This effect was observed in individual cells (Fig. 2*F*) and cell aggregates (Fig. S2*B* and Movie S3). We hypothesized that internalized NPs merge with primary lysosomes and damage the membranes of phagolysosomes (secondary lysosomes). We therefore stained granulocytes with Lysosensor green DND-189, a dye indicating pH changes in lysosomes. Incubation of granulocytes with $d_{10}$ caused early changes (20 min) in cellular morphology (Fig. 2*G*), whereas larger NPs did not affect the typical lobular nuclear morphology of granulocytes (Fig. 2*G* and Fig. S2 *C* and *D*). Furthermore, the Lysosensor dye signal decreased as determined by microscopy or flow cytometry (Fig. 2 *H* and *I*), indicating that $d_{10}$ affected lysosomes. The decreased Lysosensor signal could be due to a lysosomal pH increase or due to dilution of the dye after cell swelling. Because the signal integrates both of these possible effects, the observed time-dependent decrease of the Lysosensor mean fluorescence intensity signal in Fig. 2*I* suggests an absolute loss of signal caused by pH change.

In line, when we isolated granulocytes from air pouches of mice and incubated them with small NPs ($b_{40}$), we also noticed a reduction of the Lysosensor signal (Fig. 2*J*). Pretreatment of the donor mice with chloroquine (CQ), an antimalarial drug that prevents acidification of lysosomes (21), expectedly caused a reduced Lysosensor signal (Fig. 2*J*). Simultaneous addition of both agents even enhanced the effect. Cyclodextrin (CD) is known to destabilize lysosomes by depleting membranes from cholesterol (22). Stimulation of granulocytes by small NPs ($b_{40}$) in the presence of lysosomotropic agents showed that CQ and, to a lesser extent, CD increased the externalization of chromatin (Fig. 2*K*) and the formation of aggNETs (Fig. 2*L*) in vitro. Further evidence for NP-induced NETosis came from fast chromatin decondensation (decreased Hoechst 33342 staining; Fig. S2*E*) and increased nuclear area (Fig. S2*F*) during loss of Lysosensor signal. At a later time point (1 h), when all cells had undergone chromatin externalization, the lysosomes are dispersed and do not colocalize with the chromatin (Fig. S2*G*). In summary, we conclude that small NPs also damage lysosomal membranes and facilitate NETosis.

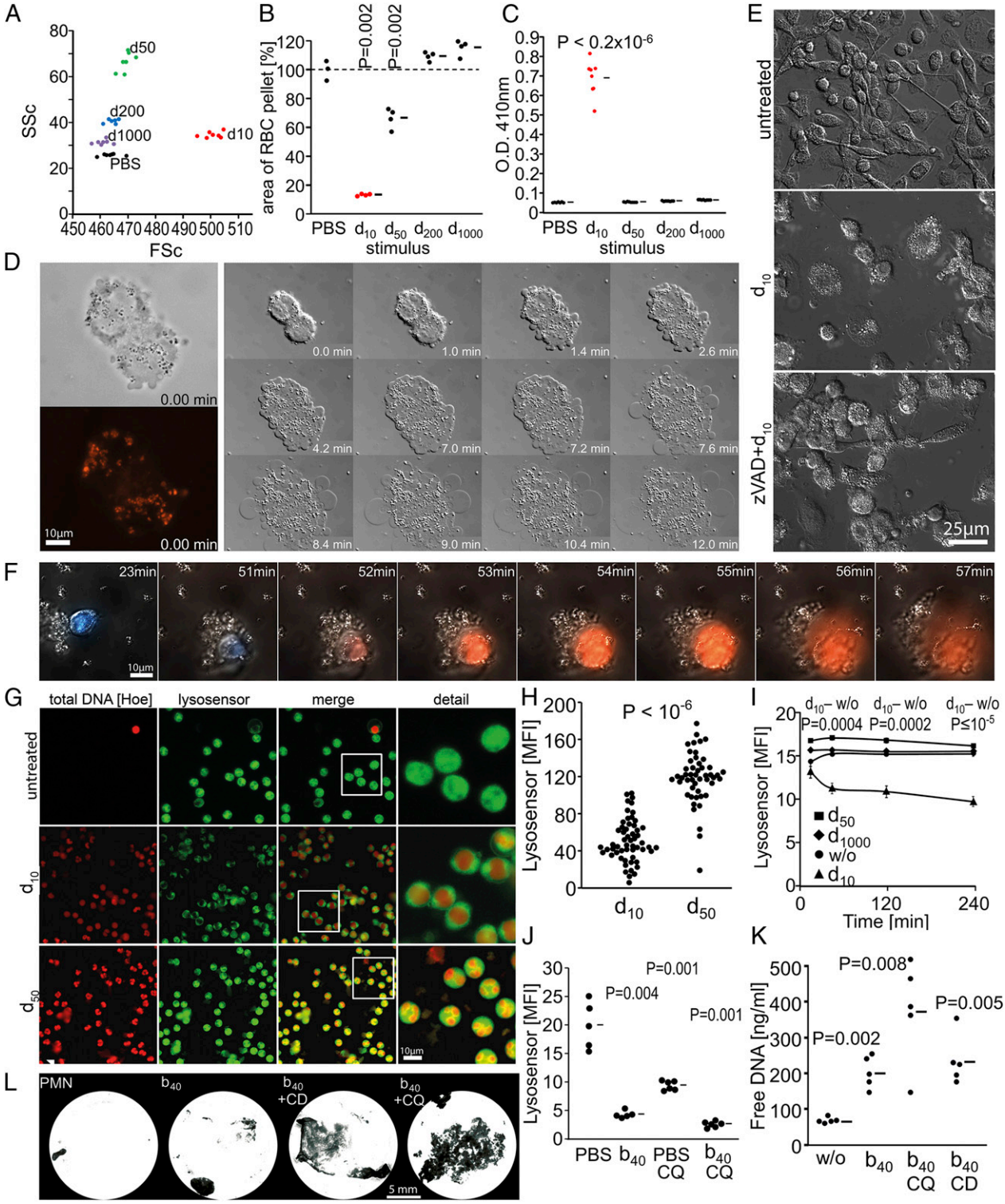


**Fig. 2.** Hydrophobic NPs size-dependently challenge cellular membranes and induce lysosomal leakage and NETosis in granulocytes. (*A*) Light scattering properties of RBCs treated with diamonds and measured by flow cytometry. SSc, side scatter. (*B*) Size of the RBC pellet after treatment with diamonds. (*C*) Hemoglobin release by RBCs after treatment with diamonds. (*D*) Rapid blebbing of HeLa cells after contact with $d_{10}$ observed by light microscopy differential interference contrast. The $d_{10}$ was made visible under fluorescent microscopy (orange). (*E*) Formation of membrane blebs in human monocyte-derived macrophages after incubation with $d_{10}$ as well as in the presence of the pan-caspase inhibitor Z-VAD. (*F*) Rapid PM rupture and subsequent DNA release/externalization by a single granulocyte in response to $d_{10}$. DNA was stained by Hoechst 33342 (blue, intracellular) and PI (red, extracellular). (*G*) Fluorescent microphotographs of granulocytes exposed to $d_{10}$ or $d_{50}$ and stained with Lysosensor (green) and Hoechst 33342 (red). The edge length of each white square is 60 μm. (*H*) Morphometric analysis of Lysosensor fluorescence in *G*. MFI, mean fluorescence intensity. (*I*) Time kinetics of the Lysosensor fluorescence by flow cytometry. (*J*) Lysosensor fluorescence in granulocytes obtained from air pouch lavages in response to $b_{40}$ analyzed by flow cytometry. (*K*) DNA release by granulocytes in the presence of CQ or CD in response to $d_{10}$ measured by the picogreen sensor. (*L*) Photographs of aggregated NETs formed by granulocytes treated with $b_{40}$ alone or in combination with the lysosomal enzyme secretion stimulator CQ (100 μM) or the PM disturbing agent CD (1 mg/mL).

**Size-Dependent Internalization of NPs and Subsequent ROS Production and NETosis.** Lysosomal damage is necessary to trigger chromatin externalization by granulocytes (NETosis). NETosis is induced by various types of crystals (monosodium urate, calcium carbonate, and calcium oxalate) and requires peptidyl arginine deiminase-4 activity (10, 23) and two core proteins of the necroptosis pathway: RIPK3 and MLKL (24). To understand the biological interactions of NPs with granulocytes, engulfment, NETosis, and ROS production were further analyzed. Granulocytes treated with nanodiamonds of all sizes displayed significantly elevated granularity in the FACS (Fig. 3*A*). Moreover, granulocytes treated with $d_{10}$ exhibited increased lucifer yellow stain, a fluorescent dye coingested with NPs (25) (Fig. 3*B*). These results show that smaller particles were internalized, whereas larger particles were not engulfed (Movie S4, granulocytes interact with $d_{1,000}$; Movie S5, granulocytes interact with fluorescent $b_{60}$).

Next, we examined whether ROS production of granulocytes is dependent on particle size. When granulocytes were preincubated with the cell-permeable ROS sensor dichloro-dihydro-fluorescein diacetate (DCFH-DA) and exposed to diamonds of different sizes, only $d_{10}$ induced ROS production in a dose-dependent manner (Fig. 3 *C* and *D*). Freshly isolated granulocytes stained with the membrane-permeable dye Hoechst 33342 formed cell aggregates upon incubation with particles of various sizes. Cells incubated with particles of smaller sizes ($b_{40}$ or $d_{10}$) exhibited more extracellular DNA and a more diffused appearance of the cell body compared with cells incubated with larger particles ($b_{1,000}$ or $d_{50}$) (Fig. 3*E*). The time kinetics and the dose–response for DNA externalization caused by $d_{10}$ are depicted in Figs. 3 *F* and *G*, respectively. Staining with the cell-permeant dye Lysosensor to visualize cell bodies containing organelles, as well as with the membrane-impermeant fluorescent DNA dye PI, confirmed this observation (Fig. 3*H*). We conclude that only smaller particles cause a significant disruption of the cell body accompanied by loss of membrane integrity.

NETosis can be induced by incubation with crystals or bacteria (7, 12) and is characterized by extracellular DNA decorated with NE, histones, or MPO (26). AggNET formation was observed at high granulocyte densities. The size of the aggregates correlated inversely with the particle size for both diamonds and polystyrene beads (Fig. S2*H*). DNA in aggNETs formed from $b_{40}$-treated (Fig. S2*I*) or $d_{10}$-treated (Fig. 3*I*) cells colocalized with NE. The formation of NETs thus leads to the extracellular immobilization of NPs as previously reported for other stimuli (27, 28). This entrapment of NPs by aggNETs may represent an additional biological barrier when designing NPs for drug delivery purposes. In summary, these data demonstrate that the size-dependent production of NETs and aggNETs by NPs is a rapid cellular reaction and requires particle internalization and ROS production.

**Size-Dependent Induction of Inflammation and Immune Responses by NPs.** Because NPs induce granulocyte activation, we aimed to assess their effects in living organisms. We injected 0.2 or 1 mg of nanodiamonds subcutaneously into the feet of mice and measured foot swelling over time. The $d_{10}$ caused significantly stronger paw edema than the $d_{50}$ 20 h after injection (Fig. 4*A*). However, this effect was only to be observed with the high-dose inoculum. In all cases, $d_{10}$ caused significantly stronger foot swelling than $d_{50}$ or $d_{1,000}$ (Fig. 4 *B* and *C*). The edema faded thereafter and almost resolved between days 9 and 17 after injection. After 19 d, microcomputed tomography (μCT) scans demonstrated local areas of bone remodeling in the paw injected with 1 mg of $d_{10}$ (three of four mice) but not $d_{1,000}$ (none of four mice) (Fig. 4*D*).

Because nanodiamonds caused local inflammation, we used $d_{10}$, $d_{10PEG}$, and $d_{1,000}$ in an ovalbumin (OVA) immunization model to elucidate their adjuvant activity. To this end, we immunized mice with OVA intraperitoneally in the absence or presence of diamonds at day 1 and day 15. The cellular immune response against OVA was evaluated by challenging the mice with OVA in the footpads on day 28. The footpad swelling was recorded 24 h later as a delayed-type hypersensitivity (DTH) reaction. The paw thickness reflects the degree of antigen-specific lymphocytic infiltration. The $d_{10}$ coinjected with OVA in the immunization phase augmented the DTH reaction during antigen challenge (Fig. 4*E*). The $d_{1,000}$ and $d_{10PEG}$ showed a significantly lower cellular adjuvant activity. PEGylation of $d_{10}$ significantly reduced the immunostimulatory potential. This procedure is known to decrease hydrophobicity and only marginally influences the size of diamonds (Fig. 1*D*). Very similar results were to be observed evaluating the humoral immune responses (anti-OVA IgG) of these mice. The $d_{10}$ triggered the highest anti-OVA titers (Fig. 4*F*), which were in the range of Freund's adjuvant (complete on the first day + incomplete on the 15th day). The $d_{1,000}$ and especially hydrophilization with PEG ($d_{10PEG}$) were significantly less effective. In summary, sustained inflammatory reactions and tissue damage were triggered by the small-sized NPs, which acted like adjuvants in supporting specific humoral and cellular immune responses. In accordance, Moyano et al. (4) reported that hydrophobicity of small gold NPs was directly associated with the level of splenocyte stimulation in vitro. However, these investigators failed to show the same level of association after intravenous administration of the NPs to mice (4). Taking these data together, we find that the route of administration of NPs seems to be a major determinant of the outcome of the immune response.

**Effective Clearance of NPs in the Lungs.** The lung is permanently exposed to natural and man-made nanopowders. Because the use of nanodiamonds gave a strongly blurred background signal in the lungs, we intranasally instilled fluorescent $beads_{50}$ ($b_{50F}$) into mice and evaluated the lungs instead. When we analyzed the lung sections 24 h after instillation, we found large amounts of beads exclusively located in the vicinity of or inside professional mononuclear phagocytes (Fig. 4*G*). Thirteen days later, $b_{50F}$ had been cleared from lungs, which no longer showed signs of inflammation. Analysis of the nuclear morphology of the tissue showed that granulocytes with characteristic multilobular nuclei were virtually absent at all time points (Fig. 4*H*). We conclude that the lung, which is highly exposed to NPs, clears the particles effectively without induction of an inflammatory response. In contrast, administration of NPs directly into the tissue surmounting the natural barrier function of skin or mucosa provokes inflammation and immune responses.

**Orchestration of the Resolution of NP-Induced Inflammation by NETs/AggNETs in Air Pouches.** To study the inflammatory response to NPs in mice further, we induced an air pouch by subcutaneous injection of sterile air. This air pouch is filled with serous exudate and lined by mononuclear cells able to respond to inflammatory stimuli. Diamonds or polystyrene NPs of various sizes were injected into air pouches, and the mice were killed after 1, 3, 7, or 14 d (Fig. 5*A*, scheme). Fluid was collected, and membranes were prepared for histology. Nanodiamonds and polystyrene beads aggregated on the inner surface of the air pouch (Fig. 5*A*). H&E staining of sections of the membranes revealed diamonds, seen as dark matter, in the innermost cell layer of the air pouch (Fig. 5*B*). Microscopic analysis of cryosections in the bright field confirmed localization of the diamonds within the pouch membrane (Fig. 5*C*). Areas with densely packed diamonds were associated with extranuclear DNA, indicative of the formation of NETs. PI staining showed fewer and bigger nuclei in the membranes treated with $d_{10}$ compared with bigger NPs (Fig. 5*C*, *Lower*, and Fig. S2*J*). The aggregation of diamonds might be mediated by the formation of aggNETs, because diamonds in the

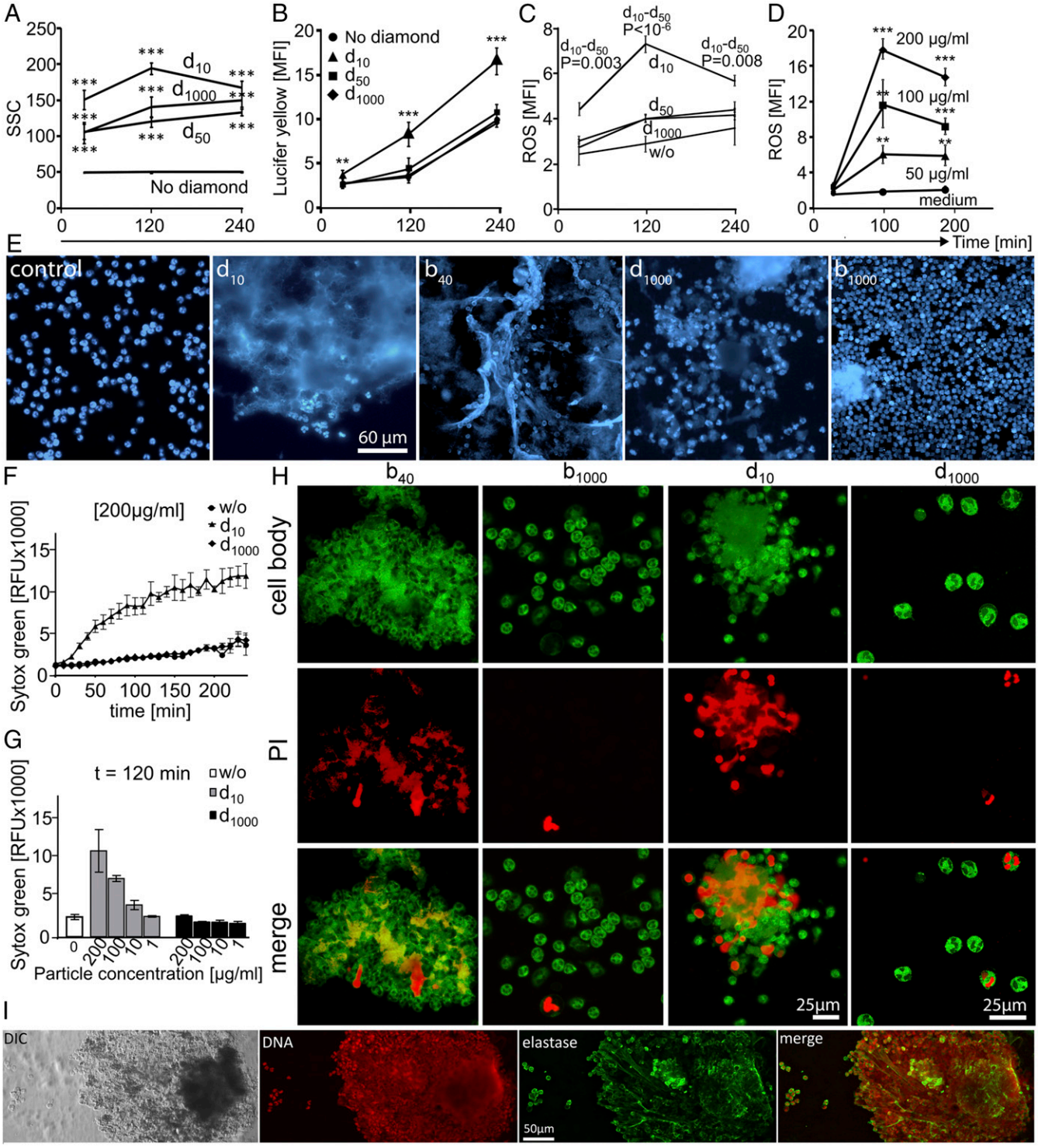


**Fig. 3.** In vitro contact of nanodiamonds and polystyrene nanopowders with granulocytes size-dependently induces engulfment, ROS production, and NETosis. (*A*) Effect of treatment of granulocytes with nanodiamonds on cellular granularity as indicated by SSc signal after the indicated coincubation time (***$P < 0.0001$ after the *t* test compared with no diamond). (*B*) Incubation of granulocytes with diamonds of various sizes in combination with lucifer yellow. Engulfment is indicated as an increase in the MFI for lucifer yellow (***$P < 0.0001$ after the *t* test comparing $d_{10}$ against all). (*C*) ROS production of granulocytes incubated with diamonds of various sizes as indicated by an increase in DCFH-DA signal. (*D*) Dose-dependent ROS production by granulocytes incubated with $d_{10}$ as indicated by increasing DCFH-DA signal (***$P < 0.0001$ after the *t* test compared with medium). (*E*) Granulocyte cultures incubated for 30 min with nanodiamonds and polystyrene beads of various sizes stained for DNA (Hoechst 33342). (*F*) Time kinetics of DNA externalization after coincubation with $d_{10}$ measured with the fluorescent probe Sytox green. RFU, relative fluorescent units; w/o, without. (*G*) Dose–response of DNA externalization by granulocytes exposed to nanodiamonds. (*H*) Granulocyte cultures treated nanodiamonds and polystyrene beads of various sizes for 30 min. Cultures stained for extracellular DNA with PI and cytoplasm (Lysosensor). (*I*) Microphotographs of aggNETs generated after coincubation of granulocytes and $d_{10}$ stained with Hoechst 33342 and NE (Cy5). DIC, differential interference contrast.

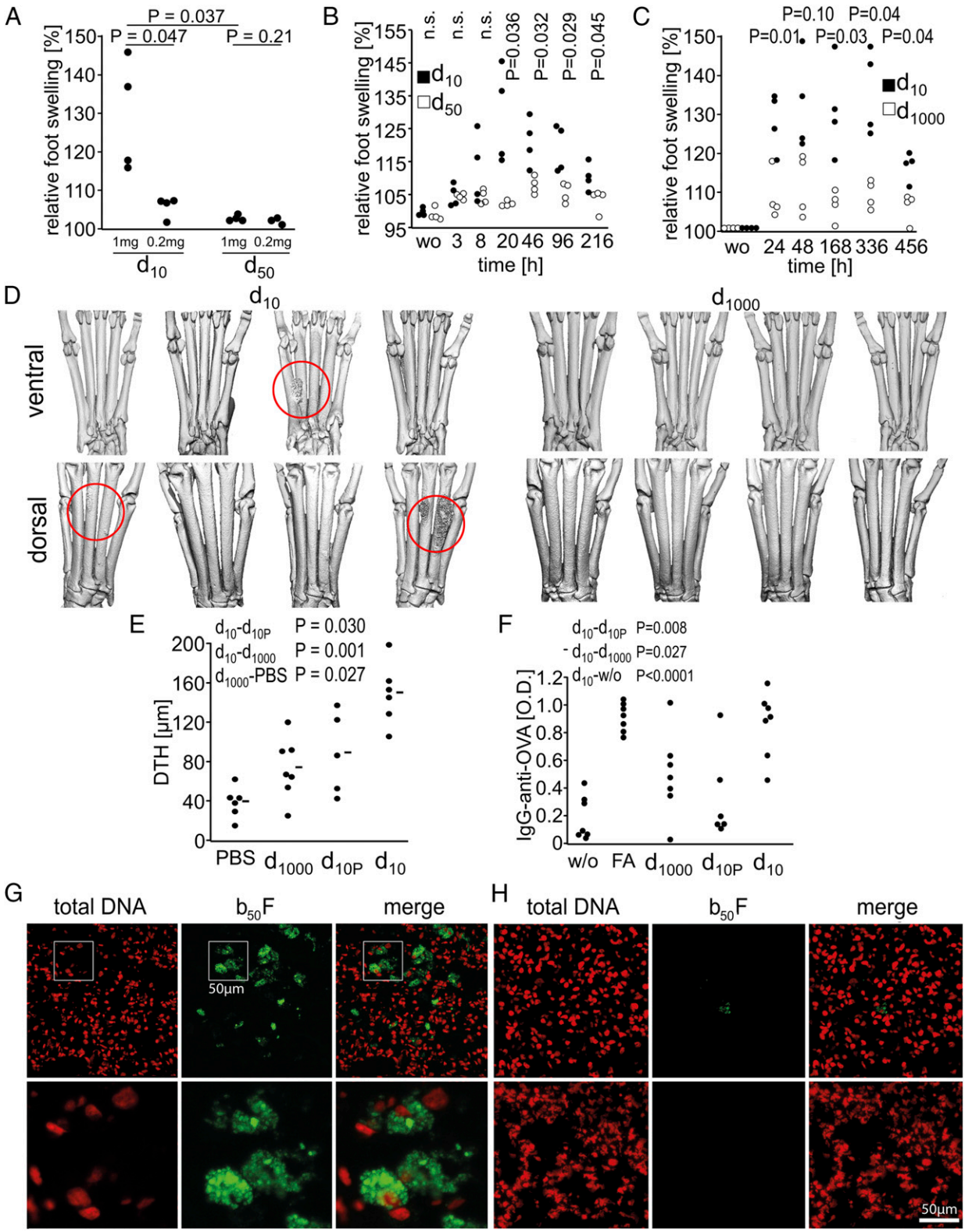


**Fig. 4.** Nanodiamonds size-dependently induce inflammation in vivo. (*A*) Foot swelling elicited by subcutaneous injection of 1.0 and 0.2 mg of nanodiamonds into the feet of BALB/c mice after 20 h. (*B*) Short-term time kinetics of foot swelling elicited by subcutaneous injection of 10-nm (●) and 50-nm (○) diamonds. wo, without. (*C*) Long-term time kinetics of foot swelling elicited by subcutaneous injection of 10-nm (●) and 1,000-nm (○) diamonds. (*D*) Three-dimensional reconstructions of μCT scans of metatarsal bones of feet injected with nanodiamonds. Bone structural changes are highlighted with red circles. (*E*) DTH reaction against OVA in mice immunized with the antigen in the presence of nanodiamonds or PEGylated nanodiamonds ($d_{10P}$). (*F*) Anti-OVA titers in mice immunized with the antigen in the presence of nanodiamonds or Freund's adjuvant (FA). (*G*) Representative microphotographs of lung cryosection 24 h after intranasal instillation with fluorescent nanobeads ($b_{50}F$), counterstained with PI. (*H*, *Upper*) Lung cryosection 14 d after intranasal instillation with fluorescent polystyrene nanobeads. (*H*, *Lower*) Lung cryosection of an untreated mouse.

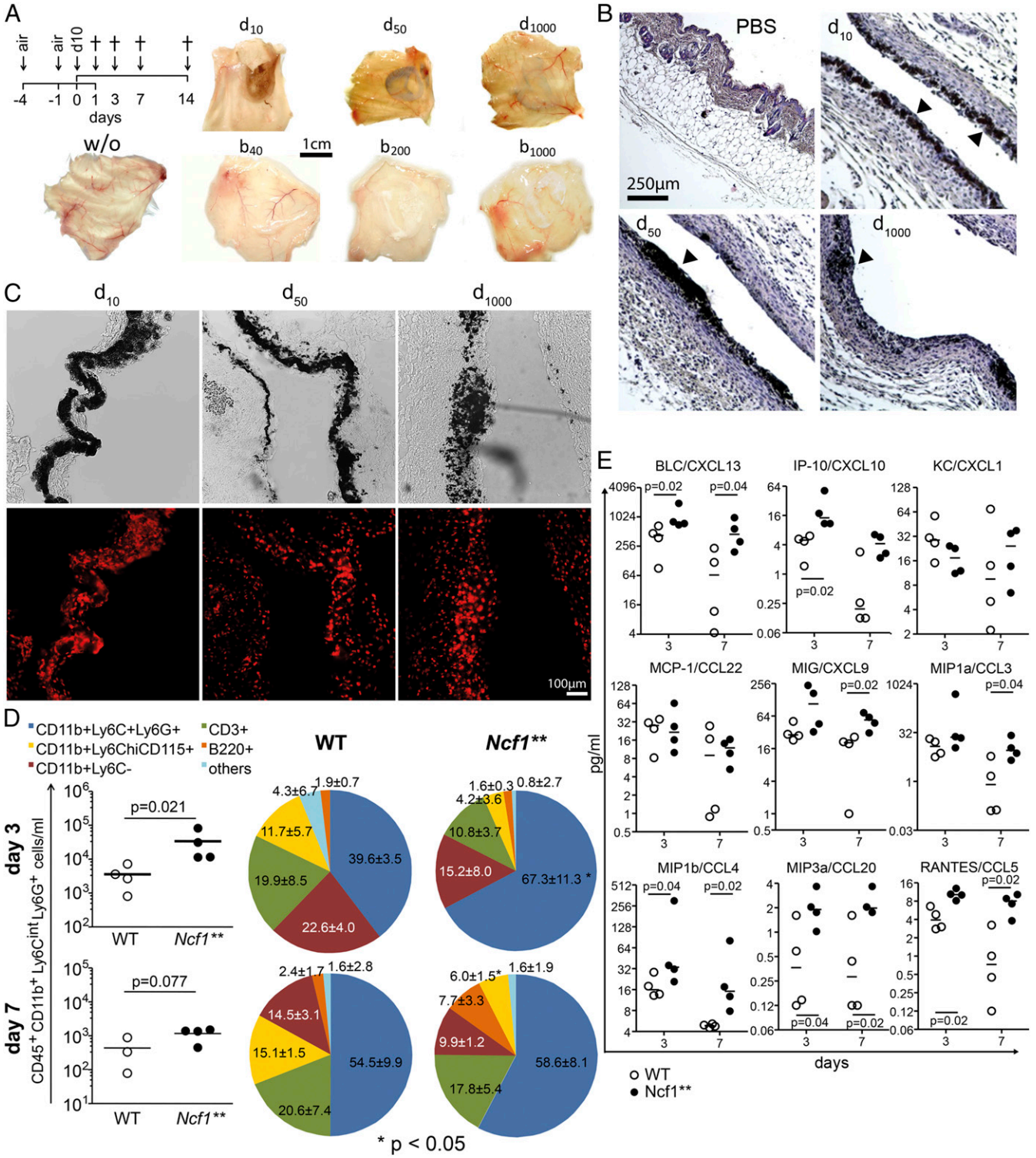


**Fig. 5.** NET/aggNET formation orchestrates the resolution of inflammation induced by nanodiamonds in air pouches. (*A*) Scheme of the generation of air pouches by subcutaneous injection of air and inflammation triggered by nanopowders and air pouches dissected 1 d after injection of 1 mg $d_{10}$, $d_{50}$, or $d_{1,000}$ or $b_{40}$, $b_{200}$, or $b_{1,000}$, respectively. (*B*) Microphotographs of air pouch paraffin sections (1 µm) 1 d after diamond injection stained with H&E. (*C*) Bright-field and fluorescence (PI) microphotographs of air pouch cryosections (2 µm) 1 d after diamond injection stained with PI. (*D*) Granulocyte numbers and subpopulation composition of air pouch lavages after $d_{10}$ injection. (*E*) Chemokine levels in air pouch lavages after $d_{10}$ injection. Statistical analysis was performed using the Kruskal–Wallis test (*$P < 0.05$, *Ncf1*** vs. WT). BLC, B lymphocyte chemoattractant; KC, keratinocyte chemoattractant; MCP-1, monocyte chemotactic protein 1; MIG, monokine induced by gamma-interferon; MIPa, macrophage inflammatory protein 1-beta; RANTES, regulated upon activation, normally T-expressed, and presumably secreted.

membrane of air pouches were surrounded by cells releasing large amounts of DNA. However, due to the specific refractory properties of the tissue-embedded diamonds, the background fluorescence in immune histochemistry was very high, making it impossible to confirm the presence of NETs by staining with antibodies against citrullinated histone H3 or NE.

Aggregated NETs degrade proinflammatory mediators by means of inherent serine proteases (12). We injected $d_{10}$ into the air pouch of WT and *Ncf1*** mice, which carry a mutation in the subunit of the NADPH oxidase 2 complex, and hence are not able to mount an oxidative burst. These mice therefore exhibit dramatically lower levels of NETosis and aggNET formation (12). The number and cell composition of infiltrating inflammatory cells of the air pouch lavages were not different 24 h after $d_{10}$ injection (Fig. S2*K*). However, after 3 d, *Ncf1*** mice exhibited increased infiltration of neutrophils in the air pouches containing $d_{10}$ compared with wild-type (WT) mice (Fig. 5*D*). Later time points (7 and 14 d) showed no differences in the size and cellularity of the infiltrate between mice strains (Fig. 5*D* and Fig. S2*K*). The increased infiltration of neutrophils in *Ncf1*** mice at day 3 was accompanied by elevated levels of the chemokines CXCL13, CCL4, CCL5, and CCL20 targeting mononuclear cells (Fig. 5*E*). This milieu persisted and was enriched by CXCL9 and CCL3 at day 7. The cytokine composition of the lavages of air pouches was not different between mouse strains until day 14, when the concentrations of IL-6 and MIP-1α were found to be significantly lower in WT mice (Fig. S2*L*). These findings suggest that proteolytical degradation of chemokines by NE present in aggNETs occurred in WT animals, thus conditioning less severe infiltrates. With this model, we finally confirmed in vivo that small NPs induce an initial inflammatory response with substantial neutrophil infiltration and that in the absence of aggNET formation, the inflammatory response cannot be properly resolved.

## Summary

NPs size-dependently trigger granulocyte activation and NETosis. This process allows entrapment of NPs in NETs and initiates a short-term inflammatory response endowed with an intrinsic mechanism for the resolution of inflammation. Based on our data, we propose that small-sized NPs disturb barrier function and ion selectivity of external and internal cellular membranes. Consequently, low-molecular-weight mediators distribute freely between the cellular compartments (Fig. S3). The phagolysosome formed when damaged membranes are engulfed for recycling and fused with primary lysosomes (Movie S6). Rupture of the latter increases ROS production and activates further intracellular pathways, which finally lead to decondensation and externalization of chromatin. The body has two strategies to cope with NPs trespassing natural barriers: in the lung, NPs are immediately taken up by mononuclear phagocytes and cleared within 2 wk without inducing signs of overt inflammation. In contrast, NPs penetrating the body's tissues become immobilized by interstitial aggNETs. The containment of the NPs in these neutrophil-derived aggregates and the proteolytical degradation of proinflammatory mediators by NET-bound serine proteases temporally and spatially restrict the initial response and orchestrate the resolution of local inflammation.

## Materials and Methods

**Preparation of Human Material.** All analyses of human material were performed in full agreement with institutional guidelines and with the approval of the Ethical Committee of the University Hospital Erlangen (permit 193_13B), which included the collection of informed consent from volunteers. Human granulocytes were isolated from heparinized (20 $U \cdot mL^{-1}$) venous blood of normal healthy donors by Lymphoflot (Bio-Rad) density gradient centrifugation. The granulocyte-rich layer on top of RBCs was taken and subjected to hypotonic lysis of RBCs. Viability was assessed by trypan blue exclusion. Human serum for complement activation studies was obtained by centrifugation of fresh drawn peripheral blood after spontaneous clotting.

**Mice.** *Ncf1*** mice, characterized by a point mutation in the *Ncf1* gene (29), originated from The Jackson Laboratory and were backcrossed over more than 10 generations to the BALB/c background and maintained at the animal facilities of the University of Erlangen or University of Lviv, respectively. The animal studies were approved by the local ethical committees and conducted according to the guidelines of the Federation of European Laboratory Animal Science Associations. Genotyping of *Ncf1*** and WT littermates was done by pyrosequencing as described previously (30). All experiments were performed using age- and sex-matched littermate controls. Estimated necessary sample sizes were biometrically determined.

**Analysis of DNA Externalization, NETosis, and AggNET Formation by Granulocytes.** Isolated granulocytes were cultured in 24-well culture plates at $1 \times 10^8$ cells per milliliter, $2 \times 10^7$ cells per milliliter, or $5 \times 10^6$ cells per milliliter with 200 $\mu g \cdot mL^{-1}$ nanodiamonds or polystyrene beads for 30 min at 37 °C unless otherwise indicated. All cultures were performed in Ringer's solution in the absence of serum. Cytospin preparations were used unless otherwise indicated. Nuclear and extranuclear DNA were stained with 1 $\mu g \cdot mL^{-1}$ Hoechst 33342 (Molecular Probes) or 1 $\mu g \cdot mL^{-1}$ PI (Invitrogen), respectively, for 30 min. DNA externalization in granulocytes cultures was quantified with the fluorescent probe Sytox green (Life Technologies). Correction for fluorescence absorption or autofluorescence induced by nanodiamonds was achieved by using $2.5 \times 10^6$ heat-necrotized granulocytes per milliliter alone or with $d_{10}$ or $d_{1,000}$. Fluorescence microscopy using standard filter sets was used. Macrophotography was performed using a Nikon D800 reflex camera.

**Histology, Immunohistochemistry, and Cytology.** Tissue samples were fixed overnight in 4% (vol/vol) formalin, and embedded in paraffin after sequential dehydration with ethanol. Paraffin sections were stained with H&E. Cytospins were performed by centrifugation of $2 \times 10^5$ granulocytes at $960 \times g$ for 10 min in a cytospin cuvette on glass slides (ThermoFisher). For cytospin and cryosection preparations, we stained DNA in NETs with Hoechst 33342 or PI at 1, 4, or 10 $\mu g \cdot mL^{-1}$, respectively, for 30 min.

**SEM of Granulocytes in the Presence of NPs.** Granulocytes for SEM were attached onto glass substrates and were prepared by sequential dehydration with ethanol. Additionally, the specimens were sputtered with a thin layer of platinum (5 nm), using a LEICA EM SCD-500 sputter coater for preparing nonconducting or poorly conducting specimens for observation in a scanning electron microscope. The surface morphology of platinum-sputtered granulocytes was recorded using a JEOL JSM 6610 scanning electron microscope at a work distance of 10 mm and with an acceleration voltage of 10 kV at room temperature.

**μCT Scanning.** μCT scanning of the metacarpophalangeal joint region was performed using an XtremeCT scanner (SCANCOMedical AG). Scans were done at a voxel size of 6.3 μm [as previously described by Stach et al. (31)] using a 70-kV energy setting. We use the same custom-made holder for all assessments. The paws were positioned in an outstretched position and fixed. The scan region was adjusted to include all metatarsal bones, with at least 1,050 slices, and the scan time was between 2.6 and 4.5 h. Three-dimensional visualization of the images was done using embedded SCANCO software.

**Air Pouch Model and Analyses of NP-Induced Paw Swelling in Mice.** We anesthetized *Ncf1*** and WT littermate mice with isoflurane and injected 3 mL of sterile air subcutaneously into the back to form an air pouch. Three days after the first injection, we injected an additional 2 mL of sterile air into the preexistent pouch. Another 2 d later, we injected 1 mg of diamonds in PBS, polystyrene beads in PBS, or PBS only into the air pouches. The pouch fluid was harvested in 1 mL of PBS at the time points indicated, and the cellularity was quantified by flow cytometry. Histological preparations of the air pouch membrane were evaluated by light and fluorescence microscopy. For analysis of paw swelling, we injected 1 mg or 0.2 mg of NPs in 50 μL of PBS subcutaneously into the foot pads of WT BALB/c mice. Paw swelling was measured with an electronic caliper by a blinded experimenter at the indicated time points.

**OVA Immunization Model.** Fifty micrograms of OVA was injected intraperitoneally in the presence or absence of 50 μg of nanodiamonds, and resuspended in 10 μL of Ringer's solution at day 1 and day 15 of the experiment. The DTH test was carried out 28 d after the first immunization by injection of 5 μg of OVA in 50 μL of Ringer's solution into the right hind paw. Injection of 50 μL of Ringer's solution into the left hind paw served as a control. The thickness of the paw before and 48 h after the injection was measured with a caliper (B110T; Kroeplin). The paw swelling was calculated by thickness of the foot 48 h after the injection minus thickness of the footpad before the injection.

**Flow Cytometry and Fluorescent Probes.** We performed all flow cytometry analyses on a Gallios flow cytometer or on a CytoFLEX flow cytometer (Beckman Coulter). Cells were stained as needed with the following fluorescent probes: lucifer yellow (Sigma); DCHF-DA (Life Technologies); Lysosensor (Life Technologies); CD11b-eFluor450 (eBiosciences); and anti–Ly6C-allophycocyanin, anti–CD45-peridinin chlorophyll protein/Cy5.5, CD115-phycoerythrin (PE), Ly6G-PE/Cy7, CD45-PE, B220-allophycocyanin, CD19-FITC, CD3-FITC, CD4-Pacific Blue, and CD8a-allophycocyanin (all from Biolegend). We used electronic compensation to eliminate bleed-through fluorescence. The data were analyzed using Kaluza 1.5 software (Beckman Coulter). Concentrations of cytokines/chemokines from supernatants or air pouch lavages were determined with the LEGENDplex Mouse Inflammation Panel (13-plex; Biolegend) and the LEGENDplex Mouse Proinflammatory Chemokine Panel (13-plex; Biolegend) or with the FlowCytomix Multiple Analyte Detection System (eBiosciences) according to the manufacturers' instructions. The data were processed with Kaluza 1.5 software.

**Evaluation of ROS Production and Lysosomal Function of Granulocytes.** ROS production by granulocytes exposed to NPs was assessed by preincubating cells with the cell-permeable ROS sensor DCFH-DA and subsequent analysis by flow cytometry. The fluorescent probe Lysosensor was used to track lysosomes in fluorescent microscope flow cytometry. The inhibitor of lysosomal acidification CQ (Sigma–Aldrich) and the cholesterol-depleting agent CD (Sigma) were used in some in vitro experiments.

**Particles.** Polystyrene beads were purchased from Polysciences, Inc., and diamonds were acquired from Schmidtz Metallography GmbH. PEGylated nanodiamonds were a kind gift from A. Demchenko (National Academy of Sciences of Ukraine). Diamond NPs were treated with NaOH and 300 °C heat before use in cultures and in animal experiments. Endotoxin content was measured for all NP preparations, and was less than 0.02 Endotoxin Units (EU)/mL or undetectable by the LAL endotoxin test (Pierce). We used DLS to monitor hydrodynamic size and surface charge of the particles. The ζ-potential, which determines the electrokinetic mobility of particles in a field gradient, also provides information about the electrostatic repulsion between particles, and is therefore related to particle stability.

**Statistical Analyses.** Results are represented as the mean ± SEM of at least three and up to eight independent experiments or the mean ± SD within a representative experiment. We performed computations and charts with SPSS PASW statistics 18 and GraphPad Prism 5.03 software. For calculation of statistical differences, we used the Student's *t* test, Kruskal–Wallis test, or Mann–Whitney *U* test, with Dunnett's post hoc test where applicable. Adjusted *P* values $<0.05$ were considered to be statistically significant.

**ACKNOWLEDGMENTS.** We thank Sabine Szunerits, Rabah Boukherroub, and Alexandre Barras (Institut d'Electronique, Microélectronique, et de Nanotechnologies, UMR CNRS 8520, Lille University 1) for their support confirming the physical properties of diamond nanoparticles; Tobias Rothe for his advice in the isolation and culture of macrophages and dendritic cells; and Irmgard Herrmann for her assistance in the preparation of photographic material and figure art. This work was supported by National Science Foundation of China Grant 81273286 (to Y.Z.). Y.Z. and M. Herrmann were supported by the International Collaborative Project in Science and Technology of Sichuan Province (2015HH0050). The German Research Council (GRC) supported Projects CRC-643-B5 and CRC-643-B8 (to M. Herrmann and G.S.), CRC-1181-C03 (to M. Herrmann and M. Hoffmann), KFO257 (to M. Herrmann), SPP 1468 Osteoimmunology IMMUNOBONE (to M. Herrmann and M. Hoffmann), and the doctoral training programs GK1660 and SFB643 (to M. Herrmann). G.S. was supported from the Innovative Medicines Initiative-funded research project Be The Cure (BTCure). C.S. was funded by the Interdisciplinary Center for Clinical Research (Grant IZKF-J41) of the University of Erlangen-Nuremberg. L.E.M. and R.B. were supported by the Pathogen and Graphene (PANG) (H2020-MSCE-RISE-2015 Project 690836). R.B. and T.D. were supported by the National Academy of Sciences of Ukraine. C.J. and R.P.F. were supported by the Bavarian State Ministry for the Environment and Consumer Protection and by the GRC through the Cluster of Excellence Engineering of Advanced Materials.

1. Grausova L, et al. (2009) Nanodiamond as promising material for bone tissue engineering. *J Nanosci Nanotechnol* 9(6):3524–3534.
2. Caputo F, De Nicola M, Ghibelli L (2014) Pharmacological potential of bioactive engineered nanomaterials. *Biochem Pharmacol* 92(1):112–130.
3. Agudo-Canalejo J, Lipowsky R (2015) Critical particle sizes for the engulfment of nanoparticles by membranes and vesicles with bilayer asymmetry. *ACS Nano* 9(4): 3704–3720.
4. Moyano DF, et al. (2012) Nanoparticle hydrophobicity dictates immune response. *J Am Chem Soc* 134(9):3965–3967.
5. Jonasson S, Gustafsson A, Koch B, Bucht A (2013) Inhalation exposure of nano-scaled titanium dioxide (TiO2) particles alters the inflammatory responses in asthmatic mice. *Inhal Toxicol* 25(4):179–191.
6. Song Y, Li X, Du X (2009) Exposure to nanoparticles is related to pleural effusion, pulmonary fibrosis and granuloma. *Eur Respir J* 34(3):559–567.
7. Brinkmann V, et al. (2004) Neutrophil extracellular traps kill bacteria. *Science* 303(5663):1532–1535.
8. Schorn C, et al. (2012) Bonding the foe—NETting neutrophils immobilize the proinflammatory monosodium urate crystals. *Front Immunol* 3:376.
9. Kirchner T, et al. (2012) The impact of various reactive oxygen species on the formation of neutrophil extracellular traps. *Mediators Inflamm* 2012:849136.
10. Desai J, et al. (2016) PMA and crystal-induced neutrophil extracellular trap formation involves RIPK1-RIPK3-MLKL signaling. *Eur J Immunol* 46(1):223–229.
11. Akong-Moore K, Chow OA, von Köckritz-Blickwede M, Nizet V (2012) Influences of chloride and hypochlorite on neutrophil extracellular trap formation. *PLoS One* 7(8): e42984.
12. Schauer C, et al. (2014) Aggregated neutrophil extracellular traps limit inflammation by degrading cytokines and chemokines. *Nat Med* 20(5):511–517.
13. Kitambi SS, et al. (2014) Vulnerability of glioblastoma cells to catastrophic vacuolization and death induced by a small molecule. *Cell* 157(2):313–328.
14. Demchenko AP (2015) Sensing inside the living cells. *Introduction to Fluorescence Sensing*, ed Demchenko PA (Springer, Cham, Switzerland), pp 603–675.
15. Blanco E, Shen H, Ferrari M (2015) Principles of nanoparticle design for overcoming biological barriers to drug delivery. *Nat Biotechnol* 33(9):941–951.
16. Anselmo AC, et al. (2015) Exploiting shape, cellular-hitchhiking and antibodies to target nanoparticles to lung endothelium: Synergy between physical, chemical and biological approaches. *Biomaterials* 68:1–8.
17. Sindhwani S, et al. (2016) Three-dimensional optical mapping of nanoparticle distribution in intact tissues. *ACS Nano* 10(5):5468–5478.
18. Chithrani BD, Chan WC (2007) Elucidating the mechanism of cellular uptake and removal of protein-coated gold nanoparticles of different sizes and shapes. *Nano Lett* 7(6):1542–1550.
19. Shen TW, et al. (2015) Distribution and cellular uptake of PEGylated polymeric particles in the lung towards cell-specific targeted delivery. *Pharm Res* 32(10):3248–3260.
20. Stylianopoulos T, Jain RK (2015) Design considerations for nanotherapeutics in oncology. *Nanomedicine (Lond)* 11(8):1893–1907.
21. Straubinger RM, Hong K, Friend DS, Papahadjopoulos D (1983) Endocytosis of liposomes and intracellular fate of encapsulated molecules: Encounter with a low pH compartment after internalization in coated vesicles. *Cell* 32(4):1069–1079.
22. Ilangumaran S, Hoessli DC (1998) Effects of cholesterol depletion by cyclodextrin on the sphingolipid microdomains of the plasma membrane. *Biochem J* 335(Pt 2): 433–440.
23. Leppkes M, et al. (2016) Externalized decondensed neutrophil chromatin occludes pancreatic ducts and drives pancreatitis. *Nat Commun* 7:10973.
24. Mulay SR, et al. (2016) Cytotoxicity of crystals involves RIPK3-MLKL-mediated necroptosis. *Nat Commun* 7:10274.
25. Schorn C, et al. (2011) Sodium overload and water influx activate the NALP3 inflammasome. *J Biol Chem* 286(1):35–41.
26. Leshner M, et al. (2012) PAD4 mediated histone hypercitrullination induces heterochromatin decondensation and chromatin unfolding to form neutrophil extracellular trap-like structures. *Front Immunol* 3:307.
27. Schorn C, et al. (2012) Monosodium urate crystals induce extracellular DNA traps in neutrophils, eosinophils, and basophils but not in mononuclear cells. *Front Immunol* 3:277.
28. Fuchs TA, et al. (2007) Novel cell death program leads to neutrophil extracellular traps. *J Cell Biol* 176(2):231–241.
29. Sareila O, Jaakkola N, Olofsson P, Kelkka T, Holmdahl R (2013) Identification of a region in p47phox/NCF1 crucial for phagocytic NADPH oxidase (NOX2) activation. *J Leukoc Biol* 93(3):427–435.
30. Hultqvist M, et al. (2004) Enhanced autoimmunity, arthritis, and encephalomyelitis in mice with a reduced oxidative burst due to a mutation in the Ncf1 gene. *Proc Natl Acad Sci USA* 101(34):12646–12651.
31. Stach CM, et al. (2010) Periarticular bone structure in rheumatoid arthritis patients and healthy individuals assessed by high-resolution computed tomography. *Arthritis Rheum* 62(2):330–339.
32. Urban CF, Reichard U, Brinkmann V, Zychlinsky A (2006) Neutrophil extracellular traps capture and kill Candida albicans yeast and hyphal forms. *Cell Microbiol* 8(4):668–676.